Propagating modes in a binary liquid mixture under thermal stress

Fabrizio Croccolo, Loreto García-Fernández, Henri Bataller, Alberto Vailati, José María Ortiz de Zárate

Propagating modes in a binary liquid mixture under thermal stress

Fabrizio Croccolo,[1,*] Loreto García-Fernández,[1] Henri Bataller,[1] Alberto Vailati,[2] and José María Ortiz de Zárate[3]
[1]*Laboratoire des Fluides Complexes et leurs Réservoirs, IPRA, UMR5150, E2S-Univ Pau & Pays Adour/CNRS/Total, 64600 Anglet, France*
[2]*Universitá degli Studi di Milano, Via Celoria 13, 20013 Milano, Italy*
[3]*Departamento de Estructura de la Materia, Física Térmica y Electrónica, Facultad de Ciencias Físicas, Universidad Complutense de Madrid, 28040 Madrid, Spain*

(Received 10 August 2018; revised manuscript received 28 September 2018; published 3 January 2019)

Nonequilibrium temperature and concentration fluctuations inside a binary liquid mixture under the action of a temperature gradient relax back to equilibrium either due to conduction and diffusion at large wave numbers, or due to the quenching determined by gravity at small wave numbers. We investigate the dynamics of nonequilibrium fluctuations in a binary liquid mixture of polystyrene and toluene heated from above under stationary conditions in a thermodiffusion experiment. We show that the strong gravitational stabilization at small wave numbers determines the appearance of propagating modes of nonequilibrium fluctuations as detected through the structure function of shadowgraph images. The propagating modes are the combined effect of temperature and velocity nonequilibrium fluctuations induced by the buoyancy force. The experimental results are in good agreement with a fluctuating hydrodynamics theroretical model including the coupling of fluctuations of velocity, temperature and concentration.

DOI: 10.1103/PhysRevE.99.012602

I. INTRODUCTION

A temperature gradient applied to a pure fluid generates a density gradient, which can lead to the onset of convection if the gradient is purely vertical, i.e., parallel to gravity, and the threshold for the Rayleigh-Bénard instability is overcome. Convection happens also if the thermal gradient has a nonzero horizontal component, without any threshold. Convection does not take place in the stable condition, i.e., below the threshold, including negative values of the Rayleigh number $\mathrm{Ra} = (\alpha g \nabla T L^4)/(\nu a_T)$ that correspond to heating the fluid from above, with $\alpha = -1/\rho(\partial\rho/\partial T)_{c,p}$ the thermal expansion coefficient, ∇T the applied temperature gradient, L the vertical thickness of the fluid layer, ν the kinematic viscosity, a_T the thermal diffusivity and ρ the density. In stable conditions the fluid is nevertheless not as quiescent as expected, because of the large enhancement of nonequilibrium (NE) velocity and temperature fluctuations [1,2]. It is particularly surprising that, for very small wave numbers q, propagating modes can be generated by the coupling of velocity and thermal fluctuations promoted by the presence of buoyancy effects. This has been theoretically predicted in the past [3], but only qualitatively verified in a rather limited number of experiments on pure fluids [4,5].

The case of a fluid mixture is more complicated due to the fact that the thermal gradient also induces, by means of the Soret effect [6–9], a concentration density gradient either parallel or antiparallel to the thermal one, which can lead to a strong amplification of nonequilibrium fluctutations determined by gravity, even by heating the mixture from above [10]. Therefore, in the case of a binary mixture it is not trivial to predict whether propagating modes exist and what mechanism induces them. So far there is no evidence of the presence of a similar mechanism in binary liquid mixtures.

In this work we show that the strong gravitational stabilization of density fluctuations in a binary liquid mixture of polystyrene in toluene heated from above determines the emergence of propagating density fluctuations at small wave numbers. We develop a fluctuating hydrodynamics theoretical model including the coupling of viscous, temperature, and concentration fluctuations in the presence of gravity, and show that its results are in good agreement with our experimental observations.

II. EXPERIMENTAL RESULTS

A thermodiffusion experiment was performed by applying a stabilizing vertical temperature difference $\Delta T = 20$ K to a layer of thickness $L = 5$ mm of a diluted polystyrene (MW = 4730 g/mol) sample dissolved in toluene at a polymer concentration $c = 2\%$ by weight. By means of dynamic shadowgraph diagnostics (see literature for details [11–15]) the behavior of NE fluctuations of both temperature and concentration is investigated, as determined by the refractive index fluctuations $\delta n = \delta c(\partial n/\partial c) + \delta T(\partial n/\partial T)$. The use of shadowgraphy to observe and analyze NE fluctuations deep inside the linear stability region, was pioneered by Wu *et al.* [16,17] for one-component fluids and by Vailati and Giglio [18] for binary mixtures.

The sample is sandwiched by two thick square sapphire windows of thickness $H_s = 8$ mm within our thermodiffusion cell. The sapphire windows are separately temperature controlled by two thermoelectric devices connected to two independent proportional-integral-derivative (PID) temperature controllers, thus allowing precise independent control of the two temperatures with an absolute accuracy of 0.01 K

*fabrizio.croccolo@univ-pau.fr

and a relative RMS stability of 0.001 K over 24 hours. This experimental scheme has been tested in many previous experiments [15,19,20].

The shadowgraph setup includes a superluminous diode (Superlum, SLD-MS-261-MP2-SM) with a wavelength of $\lambda = (675 \pm 13)$ nm, coupled to a single mode optical fiber as a light source. The diverging beam out of the fiber is collimated by using an achromatic doublet lens of focal length $f = 150$ mm positioned at a focal distance from the lens. Before and after the sample cell there are two polarizers in order to finely tune the intensity of the light impinging on the detector. No other lens is used after the sample cell, so that the image lateral size corresponds to the detector physical dimension. Here, the detector is a scientific-CMOS camera (Hamamatsu ORCA-Flash 4.0 V3) with a dynamic range of 16 bits and a resolution of 2048×2048 pixels of $6.5 \times 6.5\ \mu\text{m}^2$ placed at a distance of $z = (20 \pm 1)$ cm from the sample cell [15], therefore the detector size is $s = 1.33$ cm and the minimum wave number is $q_{\min} = 2\pi/\text{s} = 4.72/\text{cm}$. This camera allows acquiring full-frame images at a maximum frequency of $f = 100$ Hz, to be compared with what previously available in our laboratory that was limited to $f = 30$ Hz [20–23]. The fast sampling frequency allows observing fast fluctuations, such as temperature ones, as well as the propagating modes with sufficient accuracy. With the adopted optical setup it is possible to investigate wave numbers between about 5/cm and 1000/cm and timescales between 0.01 s and above 200 s.

The measurement involves the rapid imposition of a temperature difference of $\Delta T = 20$ K by heating from above. As a result, a nearly linear temperature profile is established across the sample in a "quick" thermal time of $\tau_T = L^2/a_T \cong 280$ s [24]. Eventually a concentration gradient is slowly induced by means of the Soret effect in a "slow" solutal time of $\tau_S = L^2/D \cong 8.3 \times 10^4$ s [24], i.e., almost 23 hours, where D is the fluid mass diffusion coefficient. After such time, the stationary (nonequilibrium) state is achieved and the Soret flux is exactly balanced by Fickean diffusion.

Under this condition, series of images are acquired with different sampling frequencies in order to calculate the dynamic structure function of NE fluctuations by means of the differential dynamic Algorithm, routinely used and developed in our laboratory via dedicated CUDA software [14,25,26]. In this work, images are acquired at $f = 100$, 10, and 1 Hz.

Shadowgraph images provide a visualization of the fluid layer integrated over the optical axis z. An example is provided in Fig. 1(a), showing the presence of optical inhomogeneities in the beam path. These inhomogeneities do not significantly affect the visualization of fluctuations that is obtained by subtracting images at different times, as is visible in Fig. 1(b) where the difference of two images taken at $\Delta t = 100$ s is shown. The contrast of the image difference is here enhanced by a factor of 30 in order to identify refractive index fluctuations. Clearly, no convective pattern is visible in the system, as it is in stable stationary conditions.

Each series contains $N = 2400$ images, thus sampling the NE fluctuations spans a maximum time of 2400 s. After calculating the structure function for each stack of images at a specific frequency, the signals are merged together to cover a time range of more than four orders of magnitude. Very long

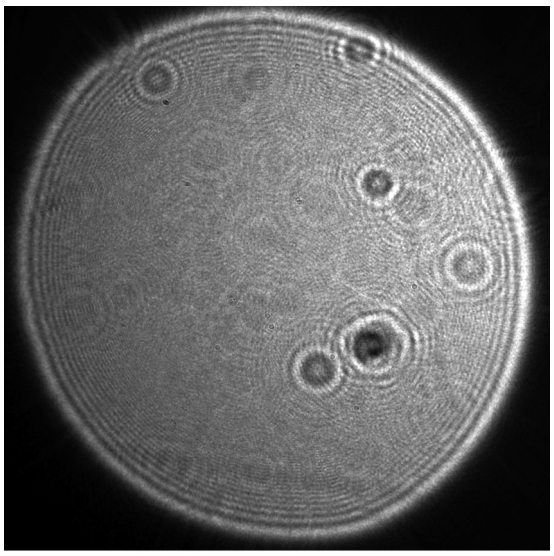

(a)

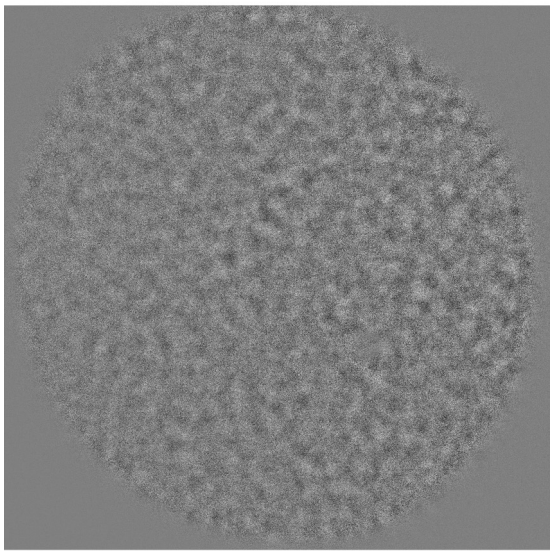

(b)

FIG. 1. (a) Sample shadowgraph image; the side of the image corresponds to $s = 1.33$ cm. (b) Difference of two images taken 100 s apart; the image contrast is enhanced by a factor of 30. Static artifacts due to finite aperture, dust in the optical surfaces, or inhomogeneous illumination, visible in (a), almost disappear upon image subtraction.

time delays larger than about 200 s are disregarded because of poor signal-to-noise ratio. Examples of the calculated structure functions are provided in Fig. 2 for different wave numbers as filled black circles.

As is visible in Fig. 2, different features appear for different wave numbers. It is worth noting that the calculated structure function is directly related to the time correlation function of NE refractive index fluctuations and the response of the optical setup by [25,27]

$$C_m(q, dt) = 2\{S(q)T(q)[1 - I_{SF}(q, dt)] + B(q)\}, \quad (1)$$

where $S(q)$ is the static power spectrum of NE fluctuations, $T(q)$ the shadowgraph transfer function [12,13], $I_{SF}(q, dt)$

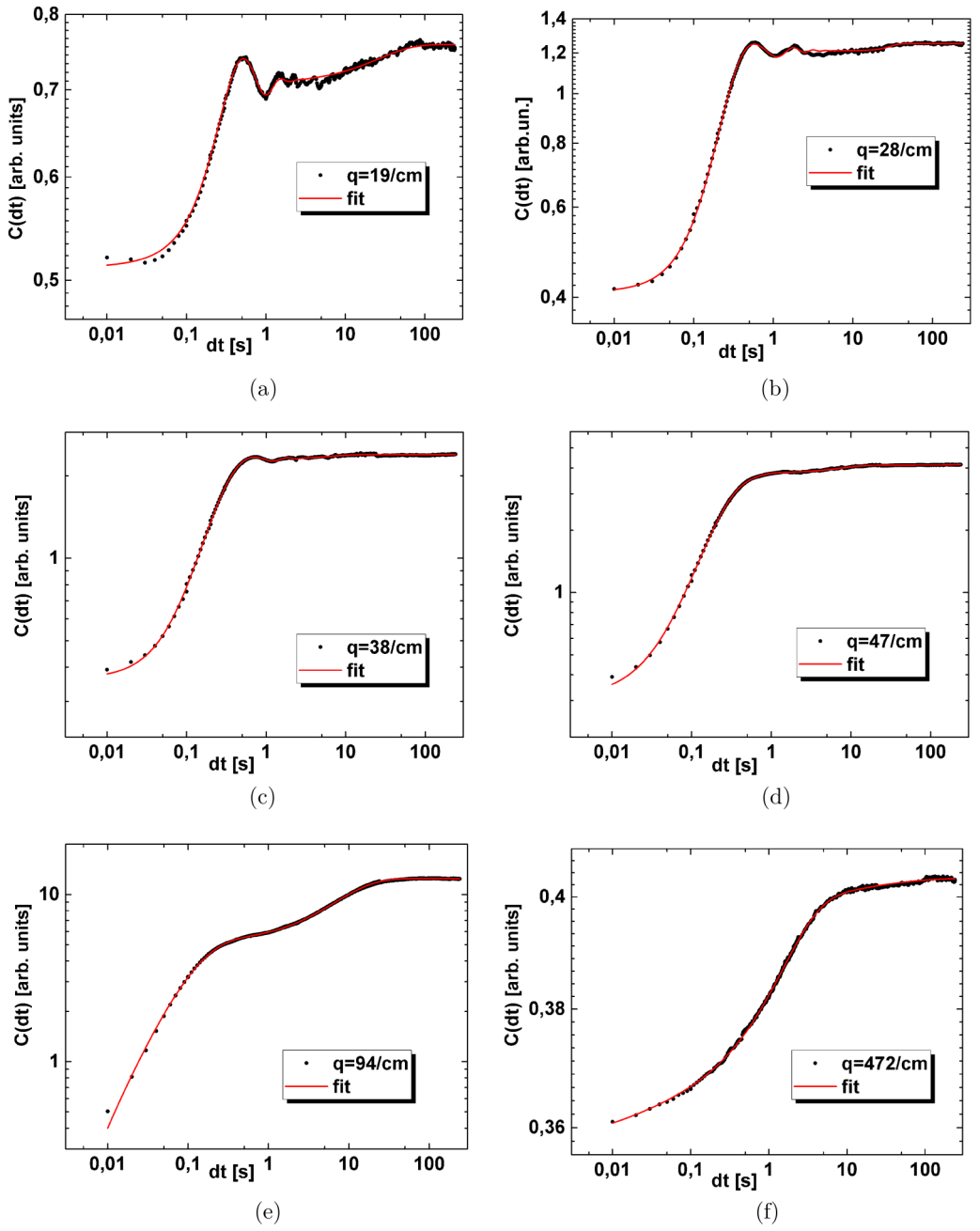

FIG. 2. Structure functions for different wave numbers. Black circles are for the experimental data points, while solid lines are for the corresponding fitting through Eqs. (1)–(3).

the normalized intermediate scattering function, and $B(q)$ a background noise, mainly related to the electronic noise of the acquisition chain. In accordance with the two dynamic regimes described later in Sec. III, at large q uncorrelated NE fluctuations of temperature and concentration are observed simultaneously, hence the I_{SF} can be modeled by the sum of two exponential decays [28]:

$$I_{SF}(q,dt) = a_1 \exp[-dt/\tau_1(q)] + (1-a_1)\exp[-dt/\tau_2(q)], \quad (2)$$

where the smallest time constant is the inverse of the decay rate of temperature fluctuations, while the largest one is the inverse of the decay rate of concentration fluctuations. Here, it is assumed that the viscous mode is not observable as a pure mode.

At smaller values of q, when propagating modes are present as visible in Figs. 2(a), 2(b), and 2(c), a sinusoidal term needs to be additionally included to describe the oscillations of the I_{SF}:

$$I_{SF}(q,dt) = a_1 \exp[-dt/\tau_1(q)] + \frac{1-a_1}{\cos[\phi(q)]} \times \cos[\Omega(q)dt + \phi(q)]\exp[-dt/\tau_2(q)], \quad (3)$$

where Ω is an oscillation frequency and ϕ a phase term, both depending on the wave number q. In Fig. 2, the experimental structure functions are fitted through Eq. (1) (solid red lines).

In accordance with the theoretical framework reported in the next section I_{SF} is modeled by Eq. (3) for small wave numbers ($q < 100/\text{cm}$) and by Eq. (2) for large wave numbers ($q > 100/\text{cm}$). For very small wave numbers such as $q = 19/\text{cm}$ and $38/\text{cm}$, where the three modes are coupled, oscillations are clearly visible and the fitting including the sinusoidal term is able to capture the oscillatory behavior. For larger wave numbers the oscillations gradually disappear, as expected, due to the decoupling of the three modes. For intermediate wave numbers between $50/\text{cm}$ and $100/\text{cm}$, both equations are used to fit data points and the difference between the resulting curves becomes less and less visible. The threshold wave number is estimated later in the text at $q_p \approx 50/\text{cm}$.

III. THEORETICAL FRAMEWORK

We consider a binary liquid mixture bounded by two plane parallel walls, which are perpendicular to gravity and separated by a distance L. When keeping the bounding planes at two different temperatures, if the various thermophysical properties are assumed as constants, a linear temperature profile appears and the system will be subjected to a stationary temperature gradient ∇T parallel to gravity. Thermodiffusion, thus, will induce a concentration gradient until a nonequilibrium stationary state is reached, where the total mass flux of Soret separation and Fickean diffusion becomes zero. In this condition the two gradients are not independent and are related by $\nabla c = -c_0(1-c_0)\, S_T\, \nabla T$, where c_0 is the average concentration of the denser component and S_T the Soret coefficient of the fluid mixture.

The question of the stability of this quiescent (nonconvective) stationary state with linear concentration and temperature profiles has been examined over the years by several authors [29–31]. For given D, a_T, and ν, stability depends on two dimensionless numbers: the separation ratio $\psi = c_0(1-c_0)S_T\beta/\alpha$ and the solutal Rayleigh number

$$\text{Ra}_\text{s} = \beta g \frac{\nabla c L^4}{\nu D} = \text{Ra}\,\psi\,\text{Le}, \tag{4}$$

with $\beta = 1/\rho(\partial\rho/\partial c)_{T,p}$ the solutal expansion coefficient. In general, both ψ and Ra_s can be positive or negative. For the purpose of this paper we do not need to review all the details of the stability region in the $\{\psi, \text{Ra}_\text{s}\}$ plane, which depend critically on the boundary conditions at the bounding plates. We just emphasize that for any positive ψ and negative Ra_s, i.e., when the density gradient is stabilizing (heavier at the bottom), the quiescent stationary state is linearly stable [29–31]. All the experiments and associated discussion in this paper refer to spontaneous fluctuations (thermal noise) that appear around these (approximately) linear stationary concentration and temperature profiles for $\psi > 0$ and $\text{Ra}_\text{s} < 0$, i.e., deep into the stability region of the quiescent state. In this situation gravity rapidly damps any fluctuations, but we are still able to observe how they decay. In none of our experiments did we observe convection, which is readily identifiable with the shadowgraph setup. Our present paper is not related to convection, or to the spatiotemporal patterns appearing when the stability of the quiescent state is lost [31].

According to the fluctuation-dissipation principle, the spatiotemporal evolution of the fluctuations around the convection-free quiescent state will be described by the same equations governing its stability [1,31]. Since we are only considering situations deep into the $\{\psi > 0, \text{Ra}_\text{s} < 0\}$ linear stability region, nonlinear effects can be ignored. Moreover, as further elaborated below, confinement (boundary conditions) only has a limited effect (unlike when the convection threshold is approached) so that it is ignored here, and following previous works a full three-dimensional spatial Fourier transformation is applied [1,3]. Then, in a first approximation, fluctuations in concentration, δc, temperature, δT and the velocity component parallel to gravity, δv_z, are coupled by buoyancy and the stationary gradients, and the resulting evolution equations in dimensionless form can be expressed as [1]

$$\frac{\partial}{\partial t}\begin{bmatrix}\delta v_z(t,\mathbf{q})\\ \delta T(t,\mathbf{q})\\ \delta c(t,\mathbf{q})\end{bmatrix} = -\mathsf{G}(\mathbf{q})\cdot\begin{bmatrix}\delta v_z(t,\mathbf{q})\\ \delta T(t,\mathbf{q})\\ \delta c(t,\mathbf{q})\end{bmatrix} \tag{5}$$

with the (inverse) linear response matrix

$$\mathsf{G}(\mathbf{q}) = \begin{bmatrix}\text{Pr}\,\text{Le}\,q^2 & -q_\parallel^2/q^2 & q_\parallel^2/q^2\\ -\text{Ra}_\text{s}\text{Pr}\,\text{Le}/\psi & \text{Le}\,q^2 & 0\\ \text{Ra}_\text{s}\text{Pr}\,\text{Le} & \psi\,q^2 & q^2\end{bmatrix}. \tag{6}$$

In these equations, space is measured in units of L and time in units of L^2/D; while the thermal expansion coefficient, α, and the solutal expansion coefficient, β, are used to define dimensionless temperature and concentration, respectively. Fourier variable $\mathbf{q}$ indicates the wave vector of the fluctuations, while $q_\parallel^2 = q_x^2 + q_y^2$ is its component parallel to the walls (perpendicular to the gradients). The other (dimensionless) parameters appearing in Eq. (6) are the Prandtl number, $\text{Pr} = \nu/a_T$, and the Lewis number, $\text{Le} = a_T/D$, which are always positive.

Physical optics theory of shadowgraphy [12] shows that experimental signals are obtained upon integration of the fluctuating fields over the height of the layer. Since in the shadowgrah experiments discussed here the height of the layer is several times the spatial resolution (see below), integration over the height is approximately equal to effectively taking $q_\perp \simeq 0$ [1,32]. Hence, for the rest of this paper the approximation $q_\parallel \simeq q$ applies. The range of wave vectors we investigate is roughly between 5 and $500/\text{cm}$. This corresponds to angles in the range 0.05 to 5 mrad, for which the approximation $q_\parallel \simeq q$ is largely valid.

Deep into the stability region, confinement (boundary conditions) effects on fluctuations manifest when the spatial size of the fluctuation becomes comparable to L. Hence, Eqs. (5) and (6) will be only valid for wave numbers larger than a few times L^{-1}. Indeed, previous investigations with a slower camera [22,22,33], for which temperature fluctuations were unobservable since they decay faster than the old camera acquisition time, showed that confinement effects on

concentration fluctuations appeared at wave numbers $q \lesssim 5.11/L$.[1] Recall from Sec. II that our shadowgraph setup has a minimum observable wave number $q_{\min} \simeq 5/\text{cm}$, as given by the pixel size. For this investigation we have selected a cell height $L = 0.5$ cm so that measurements can be considered as free from confinement effects.

Next, to solve Eq. (5) for the fluctuations, one has to compute the eigenvalues and eigenvectors of the matrix $\mathsf{G}(\mathbf{q})$ of Eq. (6), the so-called evaluation of the hydrodynamic modes. The (dimensionless) decay rates $\Gamma_i(\mathbf{q})$ of the fluctuations are given by the three roots of the determinant of the matrix:

$$\det[\mathsf{G}(\mathbf{q}) - \lambda \mathbf{1}] = [\Gamma_\nu(\mathbf{q}) - \lambda][\Gamma_T(\mathbf{q}) - \lambda][\Gamma_c(\mathbf{q}) - \lambda]. \tag{7}$$

Such a determinant is a cubic polynomial in the variable λ. By making use of the formulas for the roots of a cubic equation, one can obtain analytical expressions for the three decay rates as a function of the wave number. Since the cubic equation has real coefficients, its roots will be either three real numbers, or a real number and a pair of complex conjugates.

We note that, for the case $\{\psi > 0, \text{Ra}_s < 0\}$ under consideration here, congruent with the stability of the quiescent state [29–31], the real part of the three eigenvalues is always positive, independently of the wave number q. But, regarding the imaginary part, a thorough numerical investigation shows that the general behavior of the hydrodynamic modes as a function of q can be separated into two regions:

(1) For large q, the three modes are diffusive (real decay rates). The eigenvector of the slowest mode (with dimensionless decay rate q^2) contains fluctuations in δc only and represents a purely mass diffusion mode. The eigenvector of the fastest mode (with dimensionless decay rate $\text{Pr}\,\text{Le}\,q^2$) contains fluctuations in δv_z only and represents a purely viscous mode. The eigenvector of the intermediate mode (with decay rate $\text{Le}\,q^2$) contains in general a mixing between δT and δc, but in the limit $\text{Le} \gg (1 + \psi)$ the δc component vanishes and can be identified with a purely thermal diffusion mode. This situation has been implicitly assumed in Eq. (7). This behavior actually persists for any wave number in the absence of gravity, as it was tested for binary mixtures through the microgravity experiment GRADFLEX [21,33,34] and it will be tested for ternaries in the microgravity experiment Giant Fluctuations of the European Space Agency [35].

(2) For small q the three modes mix, and the eigenvectors become a combination of concentration, temperature, and wall-normal velocity fluctuations. This mixing also implies the appearance of propagating modes, i.e., a pair of complex conjugate eigenvalues exists. That is, two of the modes merge, the decay rates (real parts of the eigenvalues) being equal, while the presence of nonzero imaginary parts of opposite sign implies that the corresponding time correlation function becomes oscillatory.

How modes couple at finite q depends on parameter values. For ordinary liquid mixtures, where $\text{Le} > \text{Pr}$ and both are larger than unity, while the separation ratio $\psi \simeq 1$, the mode corresponding to mass diffusion at large q continues to be diffusive up to $q \to 0$, while the other two modes merge and become propagative for wave numbers below a threshold value q_p. Values of q_p which depend on Le, Pr, and ψ, can in general be only obtained numerically. More details on the behavior of the decay rates will be presented later, in the discussion of the experimental results, which is based on numerically solving Eq. (7). It is interesting that for ordinary liquid mixtures, analytical expressions for the first terms of a power series expansion of the decay rates as $q \to 0$ can be easily obtained, namely,

$$\begin{aligned}
\Gamma_c(q) &\cong \left[1 + \frac{\psi\,\text{Le}}{1+\psi}\right] q^2, \\
\Gamma_+(q) &\cong +\text{i}\sqrt{\frac{1+\psi}{\psi}\text{Le}\,\text{Pr}|\text{Ra}_s|} + \frac{1}{2}\text{Le}\left[\text{Pr} + \frac{1}{1+\psi}\right] q^2, \\
\Gamma_-(q) &\cong -\text{i}\sqrt{\frac{1+\psi}{\psi}\text{Le}\,\text{Pr}|\text{Ra}_s|} + \frac{1}{2}\text{Le}\left[\text{Pr} + \frac{1}{1+\psi}\right] q^2.
\end{aligned} \tag{8}$$

The $q \to 0$ limit of the oscillation frequency is given by the imaginary parts of the corresponding decay rates above. With physical dimensions they are expressed as

$$\Omega_0 = \sqrt{g\alpha\nabla T(1+\psi)}. \tag{9}$$

Although a detailed discussion of the amplitudes of the NE fluctuations (not only decay rates) is needed, it is worth noting that since the refractive index depends only on temperature and concentration, an isolated viscous mode cannot be observed through shadowgraph, or, more generically, light scattering experiments. The viscous mode can only be observed when it starts to couple with another mode, something that for ordinary liquid mixtures happens only for small q, when already merged with the thermal mode and become propagative. In practice, that means that the propagation occurs at wave numbers of the order of a few tens of $1/\text{cm}$, accessible only by the Shadowgraph technique.

We close this section by reminding the reader that the appearance, as a bulk phenomenon (independent of the boundary conditions), of propagating modes in the NE fluctuations around the stable quiescent state of a liquid has been predicted theoretically [3,4] in the past for one-component liquids. These predictions have been confirmed experimentally both by dynamic light-scattering [4] and shadowgraphy [5]. Here we are extending these results to binary mixtures, where there are some differences due to the presence of an additional concentration mode, but not radically new physical mechanisms.

IV. DISCUSSION

The results of the fitting of the structure functions provide information not only about the decay times of the NE fluctuations of temperature and concentration, but also, for wave numbers smaller than q_p, about the frequency of oscillation of the propagating mode. These results are shown

[1]Note that, to obtain this estimation, temperature fluctuations were neglected. Since this paper shows that with faster cameras temperature fluctuations can indeed be observed by shadowgraphy, the result need to be revised.

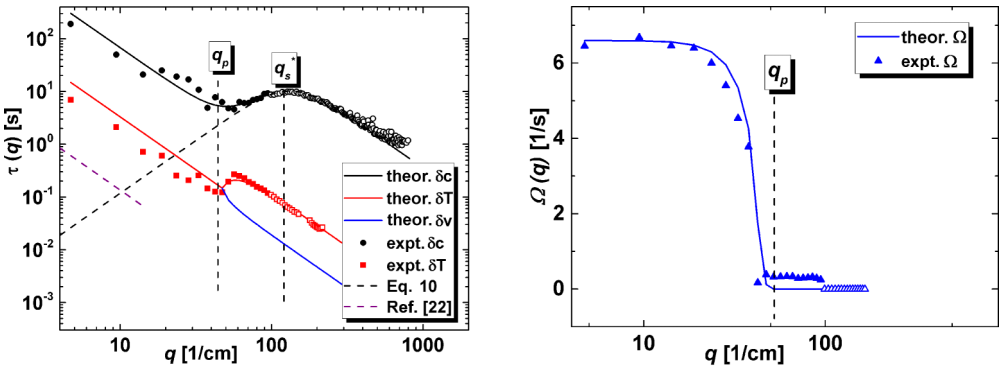

(a) (b)

FIG. 3. (a) Real part of the inverse decay rate (i.e., decay time) of (from top to bottom) concentration, thermal, and velocity modes. Data points are plotted as black circles for concentration and red squares for thermal mode. Continuous lines represent numerical calculations of Eqs. (6)–(7): the black line (top) is for the concentration, the red (middle) for the thermal, and the blue (bottom) for the viscous mode. The two dashed lines show approximated values obtained by Eq. (10) (black) or by Eq. (6) of Ref. [22] (purple, for $q < 15$/cm). (b) Dispersion curve of the coupled mode, blue triangles are for data points, while the continuous blue line is for the numerical calculations.

in Figs. 3(a) and 3(b), respectively. It is worth noting that fitting is performed through Eqs. (1) and (3) for wave numbers below 100/cm as depicted in Figs. 3(a) and 3(b) by filled markers, while is performed through Eqs. (1) and (2) for wave numbers above 100/cm as depicted in Fig. 3(a) and 3(b) by open markers. This procedure enables checking the disappearance of the oscillations in I_{SF}. Also fitting without oscillations is performed in the wave number range from 50/cm to 100/cm and results [not plotted in Fig. 3(a) and 3(b) for clarity reasons] are almost identical shortly after q_p.

As can be seen in Fig. 3(a), for very large wave numbers, time decays of temperature and concentration are well separated due to the large Le number of the chosen mixture. Furthermore, the span in time decays covers almost three orders of magnitude, thus requiring measurements in a large range of time delays, as in the experiment reported in this work.

The time decays of NE concentration fluctuations for wave numbers larger than about 50/cm well resemble the bell shape already reported in a number of previous publications [14,15,25]. The bell shape results from solving perturbatively Eq. (7) for the decay rates in powers of Le^{-1}, which is an adequate approach for liquid mixtures at moderate to large q values. The Γ_c decay rate lowest order is $\mathcal{O}(0)$, while the other two decay rates are $\mathcal{O}(\mathrm{Le})$. Reverting to physical dimensions, for the $\mathrm{Le} \to \infty$ solution for the concentration decay rate, Γ_c, one obtains the so-called bell shape:

$$\Gamma_c^{-1}(q) = \tau(q) = \frac{1}{Dq^2[1 + (q_s^*/q)^4]}, \qquad (10)$$

where $q_s^* = [\beta g \nabla c/(\nu D)]^{1/4} = (\mathrm{Ra_s})^{1/4}/L$ is the solutal rolloff wave number where the fluctuation time decays show a peak. This behavior is shown in Fig. 3(a) as a dashed black line and does not take into account any coupling with thermal or velocity fluctuations nor any confinement effect. We note that for smaller values of the wave number the decay rate of NE concentration fluctuations deviates from Eq. (10), and a clear slowing down is observed in the experimental decay times, quite similar to the one already reported for the effect of confinement [22,23,36], but for the present experiment performed with a vertical thickness $L = 0.5$ cm, no confinement effect is expected in the accessible wave vector range. The approximate values of the decay times predicted for small wave numbers by the theory including confinement but not the coupling between different modes (Eq. (6) of Ref. [22]) are shown in Fig. 3(a) as a purple dashed line. The resulting decay times are clearly rather different from our present experimental data, thus indicating that the slowing down observed here is mainly not related to confinement. Indeed, this slowing down is consistent with Eq. (8), as further discussed below.

For the NE temperature fluctuations, the peak experimentally observed in the time decays is less pronounced and no comparison to a bell shape can be performed. Nevertheless, a (thermal) diffusive behavior is observed for wave numbers larger than about 50/cm and a slowing down is observed below the same point, but no information is available for the effect of confinement on NE temperature fluctuations. From Fig. 3(a) one can appreciate that the theory predicts a sharp transition to the propagating regime, that is reflected by the experimental result. This transition is also fully apparent from the dispersion curve of the propagating modes in Fig. 3(b).

Figure 3(b) shows that the oscillation frequency is almost constant for wave numbers smaller than about 50/cm and drops to about zero around that point. After $q = 100$/cm the oscillation frequency is set to zero because the fitting is performed with Eq. (2), which does not contain the oscillatory term.

In Fig. 3(a) the results of numerically solving Eq. (7) for the decay rates are plotted as continuous curves: black for the slowest time decay (pure concentration mode at large q), red for the intermediate time decay (pure temperature mode at large q), and blue for the fastest time decay (pure viscous mode at large q). In Fig. 3(b) the blue curve represents the imaginary part of the second and third eigenvalues, an oscillatory frequency that is nonzero. As discussed in Sec. III, the decay rates are obtained as the three roots of a cubic polynomial. Therefore they can be either three real values, which happens for wave numbers larger than about 50/cm

providing three distinct modes, or one real value and a couple of complex conjugate values, which happens for wave numbers smaller than about 50/cm providing two coupled modes. In such conditions there are only two observable time decays because they are related to the real part only, but an oscillatory behavior can be observed and a (positive) oscillation frequency can be detected.

The numerical calculation is carried out by varying the four parameters Le, Pr, ψ, and Ra_s in order to fit experimental data points. The additional dimensional parameter D is utilized to get the theoretical curves fit the experimental data point. The procedure is the following. First Eq. (10) is fitted to experimental time decays of the slower mode for q larger than 50/cm thus obtaining $D = 2.8 \times 10^{-6}$ cm^2/s and $q_s^* = 132$/cm. This sets the position of the bell-shape curve shown as a dashed line in Fig. 3(a). After that, the Le number is varied to get the right time decays of the faster mode for q larger than 50/cm. Finally the two parameters Pr and ψ are varied to best fit the data, while Ra_s is kept fixed at the value obtained from q_s^* since it can be written as $\mathrm{Ra}_s = -(q_s^* L)^4 = -1.9 \times 10^7$. This procedure keeps consistency with previous publications [14,15,25], where a slower camera was used, only the concentration mode was observed, and only the bell-shape analysis was performed. Furthermore keeping Ra_s at the value obtained from the bell-shape analysis reduces the number of degrees of freedom and facilitates the full numerical fitting. The finally resulting values are Le = 310, Pr = 9.0, and $\psi = 0.18$. All the parameters obtained by fitting the experimental data with the theoretical model are in good agreement with reference data [24,33,37,38].

As can be observed in Fig. 3, the time decays provided by the numerical solution describe the experimental data points with a good agreement, especially for the concentration mode. The good agreement of the experimental results with the theory developed in this study, which does not include boundary conditions demonstrates that the slowing down at small wave numbers for both concentration and temperature fluctuations is not due to confinement effects, as also intuitively suggested by the fact that the sample is thick. This effect is thus purely related to the coupling of different modes of fluctuations. For large wave numbers the three modes of concentration, temperature, and velocity are well separated due to the large Le and Pr numbers. For wave numbers around $q = 50$/cm buoyancy affects thermal fluctuations, accelerating them so much that the thermal time decays become comparable to the viscous ones. This effect promotes the coupling of the two modes that, for smaller wave numbers, also affects the behavior of concentration fluctuations.

As is well described in a commentary by Weitz [18,39], a nonequilibrium fluctuation can be naively depicted as a volume of fluid of given size that is disposed by a vertical velocity fluctuation from its original layer into a layer of the fluid with different properties, such as temperature and concentration for a binary mixture. Focusing our attention on a concentration fluctuation (similar reasoning holds valid for a temperature one), for very large wave numbers, i.e., small volumes of fluid, the fluctuation moves from one layer to another, quickly dissipating (during the motion) the velocity gradient due to viscosity. Then, two processes contribute to the relaxation of the fluctuation, that is, Fickean diffusion and Archimedes buoyancy. For such small volumes of fluid, diffusion is the faster process and the fluctuation behavior is then entirely diffusive. This is mirrored by the time decay that is proportional to $\tau_d = 1/(Dq^2)$. For intermediate values of the wave number, fluctuations are large enough so that diffusion takes longer than buoyancy and the fluctuations are pushed back to the original layer. This is the gravity-dominated regime [40,41], characterized by time decays proportional to $\tau_g \propto q^2$ and observed in several previous publications [14,15,25].

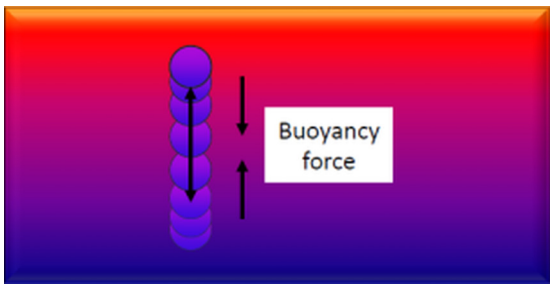

FIG. 4. Model of very large fluctuation moving under the combined effect of driving buoyancy and dissipative viscosity.

For even smaller wave numbers propagating modes occur. An intuitive explanation (beside the coupling of different modes) is that for very large fluctuations the buoyancy force is stronger than viscous dissipation such that the fluctuation is pushed even farther than the original layer, then buoyancy inverts its action to the opposite direction, as depicted in Fig. 4, and an oscillatory behavior takes place generating a propagating mode, visible as a damped oscillation in the structure function in Figs. 2(a)–2(c).

With this picture in mind, one can determine the oscillation frequency by a simple back-of-the-envelope calculation considering that the fluctuation moves in a linear density profile resulting from combined temperature and concentration profiles: $\rho(z) = \rho_0 + \nabla\rho \cdot z$, where ρ_0 is the value of the fluid density at the original layer of the displaced volume and $\nabla\rho = \nabla\rho_T + \nabla\rho_c = \nabla\rho_T(1+\psi) = \rho_0\alpha\nabla T(1+\psi)$ where $\nabla\rho_T$ and $\nabla\rho_c$ are the density gradients associated to the macrosopic temperature and concentration gradients, respectively. The buoyancy force is then given by $m(d^2z/dt^2) = [\rho(z,t) - \rho_0]gV$, and consequently the harmonic-oscillator equation $(d^2z/dt^2) = -g(\nabla\rho/\rho_0)z$ admits solutions with the oscillation frequency $\Omega = \sqrt{g(\nabla\rho/\rho_0)} = \sqrt{g\alpha\nabla T(1+\psi)}$. It is interesting to see that this simple calculation fully agrees with the $q \to 0$ limit of the complete theory, as given by Eq. (9). The value obtained by averaging the almost constant values of Ω in Fig. 3(b) is about $\Omega = 6.3$/s, very compatible with the value calculated by Eq. (9) and the available fluid properties $\Omega = 6.5$/s.

V. CONCLUSIONS

We report an oscillatory behavior in the structure function of NE fluctuations in a fluid mixture of diluted polystyrene in toluene as detected through a fully quantitative shadowgraph diagnostics. The development of the fluctuating hydrodynamics theory including fluctuations of velocity, temperature and concentration, but without including boundary conditions, and its comparison with experimental data show

that the observed effect is due to the coupling of the viscous and the thermal modes promoted by the buoyancy force. The extension of the theory corresponds to avoid negelcting the large Prandtl number approximation, as was done in the past as a good approximation for intermediate to large wave numbers. We find that the appearance of the propagating mode inducing oscillation in the structure function is accompanied by a slowing down in the time decays of temperature and concentration NE fluctuations. This slowing down is clearly not related to confinement effects, since the boundary layers are not included in the theory. Nevertheless, we note that the slowing down is common to different effects, like the coupling of viscous, thermal, and concentration modes for a binary mixture; thermal and concentration modes plus boundaries again in a binary mixture, when velocity fluctuations are neglected; and thermal and two distinct concentration modes in a ternary mixture. Further investigation is needed to fully understand the analogies among these different situations.

ACKNOWLEDGMENTS

We gratefully acknowledge support from the European Space Agency (ESA) and the Centre National d'Etudes Spatiales (CNES) of France, specifically for supporting the acquisition of the fast camera that made it possible to observe the propagating mode described in this paper. F.C., L.G.F., and H.B. would like to thank E2S-UPPA for financial support. The research at the Complutense University was supported by Grant No. ESP2017-83544-C3-2-P of the Spanish Agencia Estatal de Investigación.

[1] J. M. Ortiz de Zárate and J. V. Sengers, *Hydrodynamic Fluctuations in Fluids and Fluid Mixtures* (Elsevier, Amsterdam, 2006).
[2] F. Croccolo, J. M. Ortiz de Zárate, and J. V. Sengers, Eur. Phys. J. E **39**, 125 (2016).
[3] P. N. Segré, R. Schmitz, and J. V. Sengers, Phys. A **195**, 31 (1993).
[4] J. P. Boon, C. Allain, and P. Lallemand, Phys. Rev. Lett. **43**, 199 (1979).
[5] C. J. Takacs, G. Nikolaenko, and D. S. Cannell, Phys. Rev. Lett. **100**, 234502 (2008).
[6] C. Ludwig, Sitzungsbur. Osterr. Akad. Wiss., Math.-Nat. Kl. **20**, 539 (1856).
[7] C. Soret, Arch. Sci. Phys. Nat. Geneve **2**, 48 (1879).
[8] S. R. de Groot and P. Mazur, *Nonequilibrium Thermodynamics* (North-Holland, Amsterdam, 1962).
[9] W. Köhler and K. Morozov, J. Non-Equilib. Thermodyn. **41**, 151 (2016).
[10] F. Giavazzi and A. Vailati, Phys. Rev. E **80**, 015303(R) (2009).
[11] G. S. Settles, *Schlieren and Shadowgraph Techniques* (Springer, Berlin, 2001).
[12] S. Trainoff and D. S. Cannell, Phys. Fluids **14**, 1340 (2002).
[13] F. Croccolo and D. Brogioli, App. Opt. **50**, 3419 (2011).
[14] F. Croccolo, D. Brogioli, A. Vailati, M. Giglio, and D. S. Cannell, Phys. Rev. E **76**, 041112 (2007).
[15] F. Croccolo, H. Bataller, and F. Scheffold, J. Chem. Phys. **137**, 234202 (2012).
[16] M. Wu, G. Ahlers, and D. S. Cannell, Phys. Rev. Lett. **75**, 1743 (1995).
[17] J. Oh, J. M. Ortiz de Zárate, J. V. Sengers, and G. Ahlers, Phys. Rev. E **69**, 021106 (2004).
[18] A. Vailati and M. Giglio, Nature (London) **390**, 262 (1997).
[19] F. Croccolo, F. Scheffold, and A. Vailati, Phys. Rev. Lett. **111**, 014502 (2013).
[20] C. Giraudet, H. Bataller, and F. Croccolo, Eur. Phys. J. E **37**, 107 (2014).
[21] F. Croccolo, C. Giraudet, H. Bataller, R. Cerbino, and A. Vailati, Microgravity Sci. Technol. **28**, 467 (2016).
[22] C. Giraudet, H. Bataller, Y. Sun, A. Donev, J. M. Ortiz de Zárate, and F. Croccolo, Europhys. Lett. **111**, 60013 (2015).
[23] C. Giraudet, H. Bataller, Y. Sun, A. Donev, J. M. Ortiz de Zárate, and F. Croccolo, Eur. Phys. J. E **39**, 120 (2016).
[24] Not all fluid properties are given in literature for exactly the same fluid mixture; as "order of magnitude" values we used in the preparatory phase the following values: $a_T = 9 \times 10^{-4}$ cm^2/s [42]; $D = 1.8 \times 10^{-6}$ cm^2/s [43]; $\nu = 6.4 \times 10^{-3}$ cm^2/s [44], $\alpha = 9 \times 10^{-4}$/K, $\beta = 0.55$ [33].
[25] F. Croccolo, D. Brogioli, A. Vailati, M. Giglio, and D. S. Cannell, Appl. Opt. **45**, 2166 (2006).
[26] G. Cerchiari, F. Croccolo, F. Cardinaux, and F. Scheffold, Rev. Sci. Instrum. **83**, 106101 (2012).
[27] E. O. Schulz-DuBois and I. Rehberg, Appl. Phys. **24**, 323 (1981).
[28] I. Lizarraga, C. Giraudet, F. Croccolo, M. M. Bou-Ali, and H. Bataller, Microgravity Sci. Technol. **28**, 545 (2016).
[29] R. S. Schechter, I. Prigogine, and J. R. Hamm, Phys. Fluids **15**, 379 (1972).
[30] E. Knobloch and D. R. Moore, Phys. Rev. A **37**, 860 (1988).
[31] M. C. Cross and P. C. Hohenberg, Rev. Mod. Phys. **65**, 851 (1993).
[32] R. Schmitz and E. G. D. Cohen, J. Stat. Phys. **40**, 431 (1985).
[33] A. Vailati, R. Cerbino, S. Mazzoni, C. J. Takacs, D. S. Cannell, and M. Giglio, Nat. Commun. **2**, 290 (2011).
[34] R. Cerbino, Y. Sun, A. Donev, and A. Vailati, Sci. Rep. **5**, 14486 (2015).
[35] P. Baaske, H. Bataller, M. Braibanti, M. Carpineti, R. Cerbino, F. Croccolo, A. Donev, W. Köhler, J. M. Ortiz de Zárate and A. Vailati, Eur. Phys. J. E **39**, 119 (2016).
[36] F. Croccolo and H. Bataller, Eur. Phys. J. E **39**, 132 (2016).
[37] J. Rauch and W. Köhler, Phys. Rev. Lett. **88**, 185901 (2002).
[38] J. Rauch and W. Köhler, J. Chem. Phys. **119**, 11977 (2003).
[39] D. A. Weitz, Nature **390**, 233 (1997).
[40] A. Vailati and M. Giglio, Phys. Rev. Lett. **77**, 1484 (1996).
[41] A. Vailati and M. Giglio, Prog. Colloid Polym. Sci. **104**, 76 (1997).
[42] W. B. Li, P. N. Segré, R. W. Gammon, and J. V. Sengers, Phys. A **204**, 399 (1994).
[43] K. J. Zhang, M. E. Briggs, R. W. Gammon, J. V. Sengers, and J. F. Douglas, J. Chem. Phys. **111**, 2270 (1999).
[44] P. Vidakovic and F. Rondelez, Macromolecules **18**, 700 (1985).